

# Particles Decorated by an Ionizable Thermoresponsive Polymer Brush in Water: Experiments and Self-Consistent Field Modeling

S. P. C. Alves,<sup>\*,†</sup> J. P. Pinheiro,<sup>‡</sup> J. P. S. Farinha,<sup>†</sup> and F. A. M. Leermakers<sup>§</sup>

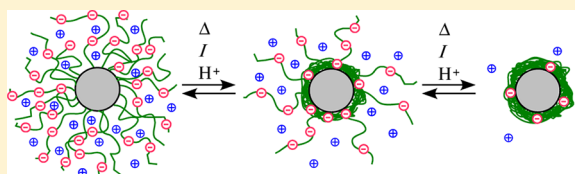
<sup>†</sup>Centro de Química-Física Molecular and IN—Institute of Nanoscience and Nanotechnology, Instituto Superior Técnico, 1049–001 Lisboa, Portugal

<sup>‡</sup>IBB/CBME, Departamento de Química e Farmácia, Faculdade de Ciências e Tecnologia, Universidade do Algarve, Campus de Gambelas, 8005–139 Faro, Portugal

<sup>§</sup>Laboratory of Physical Chemistry and Colloid Science, Wageningen University, Dreijenplein 6, 6703 HB Wageningen, The Netherlands

**ABSTRACT:** We have synthesized anionic multistimuli responsive core–shell polymer nanoparticles with low size dispersity composed of glassy poly(methyl methacrylate) (PMMA) cores of ca. 40 nm radius and poly(*N*-isopropylacrylamide) (PNIPAM) anionic brush-like shells with methacrylic acid comonomers. Using dynamic light scattering, we observed a volume phase transition upon an increase in temperature and this response was pH and ionic strength dependent.

Already at room temperature we observed a pronounced polyelectrolyte effect, that is, a shift of the apparent  $pK_a$  extracted from the degree of dissociation of the acids as a function of the pH. The multiresponsive behavior of the hydrophobic polyelectrolyte brush has been modeled using the Scheutjens–Fleer self-consistent field (SF-SCF) approach. Using a phenomenological relation between the Flory–Huggins  $\chi$  parameter and the temperature, we confront the predicted change in the brush height with the observed change of the hydrodynamic radius and degree of dissociation and obtain estimates for the average chain lengths (number of Kuhn segments) of the corona chains, the grafting density and charge density distributions. The theory reveals a rich internal structure of the hydrophobic polyelectrolyte brush, especially near the collapse transition, where we find a microphase segregated structure. Considering this complexity, it is fair to state that the theoretical predictions follow the experimental data semiquantitatively, and it is attractive to attribute the observed disparity between theory and experiments to the unknown polydispersity of the chains, the unknown distribution of the charges, or other experimental complications. More likely, however, the deviations point to significant problems of the mean field theory, which focuses solely on the radial distributions and ignores the possibility of the formation of lateral (local) inhomogeneities in partially collapsed polyelectrolyte brushes. We argue that the PNIPAM brush at room temperature is already behaving nonideally.



## INTRODUCTION

Responsive polymeric nanoparticles with well controlled size distributions are not only of academic interest, but are also considered for a wide range of applications, such as sensors, medical diagnostics or environmental remediation.<sup>1–6</sup> We have synthesized anionic multistimuli responsive core–shell particles to obtain well-defined carriers for metal ions to be used in environmental monitoring studies. In a recent paper,<sup>7</sup> some of us presented core–shell particles composed of glassy poly(methyl methacrylate) (PMMA) cores onto which a cross-linked shell was synthesized composed of poly(*N*-isopropylacrylamide) (PNIPAM) anionic chains with either acrylic acid (AA) or methacrylic acid (MA) comonomers cross-linked with *N,N'*-methylene bis(acrylamide). Here we present very similar particles with a PMMA core and PNIPAM corona where we used MA comonomers (referred to below as P(*N*-MA) particles) for which the cross-linking of the corona chains was omitted. As the corona chains are still end-grafted to the core-chains the current particles can be seen as core–shell particles of which the shell is a corona with a classical brush structure. Both the cross-linked<sup>7</sup> as well as the current brush-like particles (see below)

show a pronounced size response with temperature, pH and ionic strength. These changes were routinely recorded by measuring the hydrodynamic size in dynamic light scattering experiments. The particles also show a pronounced polyelectrolyte effect, that is a shift of the apparent  $pK_w$  for the degree of dissociation of the acid groups as a function of pH, even at room temperature.

The structure of a temperature sensitive and pH and ionic strength dependent corona can be modeled by modern statistical thermodynamical approaches. Our method of choice is the self-consistent field (SCF) theory. Originally the SCF modeling has been applied to polymers at interfaces and the predictions were collected by Fleer and co-workers in a book.<sup>8</sup> From this we know that many generic aspects of polymers at interfaces, such as the adsorbed amount, the layer thickness, or the effect on the colloidal stability can be captured semiquantitatively. In recent years, the theory has been used to describe many other

Received: August 21, 2013

Revised: December 20, 2013

Published: February 21, 2014

molecularly inhomogeneous systems. Only a few case studies have been reported for which SCF predictions were systematically compared to experiments. An early example of such a study is for polymer brushes, where it was shown that SCF modeling indeed compares favorably to experimental results.<sup>9</sup> The numerical SCF theory has been used to help the development of analytical theories, for example for polyelectrolyte brushes.<sup>10,11</sup> Truly quantitatively predictive results can only be expected when molecular details are included in the models. A nice example is how lipids organize in bilayers which compares remarkably well with all-atom molecular dynamics simulations.<sup>12</sup> Also the competition between nonionic surfactant self-assembly at the silica surface and poly(ethylene oxide) adsorption was successfully modeled by Postmus et al.<sup>13</sup> Models for spherical polyelectrolyte (PE) brushes (i.e., PE chains that are densely grafted onto spherical particles) have been studied using the classical Scheutjens–Fleer self-consistent field (SF-SCF) theory for more than a decade.<sup>14,15</sup>

Complementary scaling analysis and computer simulations provided deep understanding in the physical behavior of these systems.<sup>16,17,10</sup> The hydration of the brush is promoted by the presence of ionizable groups along the polymer chains. Here we focus on weakly charged groups for which the degree of ionization depends on the pH and then the brush height increases, that is the brush picks up more solvent, with increasing pH. The ionic strength screens the charges and this may help, for given  $\text{pH} \approx \text{pK}_a$ , the further dissociation of the chargeable groups. In low ionic strength conditions (the osmotic regime) we may observe a dissociation induced increase of the brush height with increasing salt concentration. At high ionic strengths we enter the salted brush regime, wherefore the screening results in a decrease of the brush height with increasing ionic strength. It is much easier to find systems in the salted brush regime than in the osmotic regime because the latter requires (very) low ionic strength conditions.

The hydration of PE chains is not only influenced by the charge density along the chain and the screening by salt, but also by the way water interacts with the remainder of the chains. Classically the Flory–Huggins (FH)  $\chi$  parameter is used to quantify these interactions. A high value of this parameter  $\chi > 0.5$  signals poor solvent conditions. PE's in poor solvent conditions, so-called hydrophobic polyelectrolytes, are balancing between two opposing forces. The poor solvent conditions call for a reduction of the hydration, whereas the charges call for an increase in hydration. It is this balance of forces that are responsible for the large responsiveness to the control parameters.

Water tends to be a marginal solvent for many polymers. This trend must be attributed to the strong intramolecular H-bonding properties of water and the restricted possibility for water molecules to form H-bonds with the polymer segments. Hence, in water many polyelectrolytes qualify as hydrophobic polyelectrolytes. The SF-SCF model can not take H-bonding explicitly into account. Instead it takes the already mentioned  $\chi$  parameter as an input and treats these interactions qualitatively; it replaces the directional interactions by isotropic ones. Interpreting the FH parameter as purely enthalpic, we should find an increase of solvent quality (reduction of  $\chi$ ) with increase of temperature. It appears however that with increasing temperature, the solvent quality of many polymers in water deteriorates; indeed PNIPAM has a well-known lower critical solution temperature (LCST) behavior in water. This mechanism can only phenomenologically be captured in the SF-SCF

modeling by using an *ad hoc* temperature dependence of the Flory–Huggins  $\chi(T)$  parameter.

The grafting density of chains as well as the average chain length of the corona chains in our core–shell particles is largely unknown. One of the aims of our modeling study is therefore to come up with reasonable estimates for these key quantities. However our ambitions go further. As mentioned already, the core–shell particles were characterized by dynamic light scattering (DLS) and preliminary data are available for the titration curves. The hydrodynamic size was measured as a function of temperature for a series of pH values and a few ionic strength conditions. From the synthetic protocol we know that the average charge in the chains is near 10%, but no direct information is available on the charge distribution. The degree of dissociation as a function of the pH has been measured for a few ionic strength conditions at room temperature.

From the literature we know that the reactivity of methacrylic acid (in the P(N-MA) particles) is not identical to the reactivity of N-isopropylacrylamide (NIPAM) and therefore the synthesis protocol was tuned to aim for an as homogeneous as possible distribution of charges. Still the possibility exists that in the P(N-MA) particles the negative charges might be preferentially distributed somewhat near the core of the particle. Of course, the temperature at which the volume phase transition ( $T_{VPT}$ ) takes place is affected by the electrostatics inside the particle shell and confronting the experimental data with SF-SCF predictions may give additional information on the homogeneity of the distribution of chargeable groups.

The SF-SCF theory needs a molecular model to work with. Here we will use a freely jointed chain model. In reality, however, the PNIPAM chain is not fully flexible. The standard solution of this problem is to introduce so-called statistical segments. Here we assume that there are several chemical segments grouped into one statistical segment with length 0.6 nm. Our model further ignores most of the chemistry and represents the chain as a string of amorphous beads, some of which can be chargeable. The solvent and the 1:1 electrolyte ions are considered monomeric segments. We take the ions to be ideally soluble in water and we will fully ignore specific ion effects, that is ion-specific interactions with surface or polymer segments. The polymer segments are further expected to interact similarly with the monomeric solvent species (water and ions). The motivation of such a severely simplified model is to keep the number of parameters in the model as small as possible.

On top of the idealized parameter setting, there are theoretical issues. Indeed it must be realized that the SF-SCF theory implements mean-field and lattice approximations: making use of the symmetry of the problem we identify layers of lattice sites over which the concentration of segments is averaged. In such a situation only the concentration profile (volume fraction profile) normal to these layers is available. Considering the core–shell system, it is natural to choose a spherical coordinate system, wherein the volume fraction profiles in the radial directions are the key quantities of interest. The mean-field averaging prevents us to observe any lateral or local concentration fluctuations in the corona. Indeed, when the corona is near the LCST transition the theory enforces the radial homogeneity of the corona layer. In reality the radial homogeneity is not guaranteed. For example, the chains may bundle so that the segments can largely avoid contact with water and the charged segments can still be somewhat accessible to the solvent and the ions. Such bundling has been seen in molecular dynamics (MD) simulations.<sup>18</sup> Alternatively, the partially collapsed chains may form drop-like

assemblies sitting at the surface of the core. The interactions of the corona chains for the core set the “contact angle” of these drops, complicating the picture significantly. Again, these lateral features are not accounted for in the current model. We therefore advocate that, at this stage, it is pointless to try to push the fitting of experimental results to its limits.

Now the natural question arises, how to interpret differences between the modeling and the experimental data? We can either point to the simplifications of the model or to the theoretical shortcomings. One of the possible solutions to this issue is to study how the predictions depend on variations of the model. If none of the possible variations of the model can explain the disparity between theory and experiment, it is likely that the differences are caused by shortcomings of the SFC theory. In the discussion of this paper we will sum up our attempt to explore variations of the model, and discuss how the results are a function of these variations. After that we will present our conclusions on how and why the theory falls short to completely reproduce the experimental data for the collapse of a hydrophobic polyelectrolyte brush.

The remainder of this paper is set up as follows: We will first present the molecular model and the theoretical premisses of the SF-SCF theory. This is followed by the Materials and Methods, wherein we present information on the experimental aspects of the particle synthesis and the dynamic light scattering and potentiometric experiments. In the Results, we will first discuss the structure of the corona chains in some detail before we confront theory with experiments. We conclude with a discussion, wherein we will elaborate on the possible origins of the differences found. Finally we will present our conclusions.

## ■ SF-SCF THEORY AND THE MOLECULAR MODEL USED

Here we discuss the key theoretical approximations which are relevant for the model of the corona layer used. The value of the parameters, and thus the details of the model, will be discussed separately.

Self-consistent field modeling on polymeric systems make use of the Edwards diffusion equation which evaluates the conformations of the macromolecules on a Gaussian level (or when mapped onto a lattice model -see below-, on a freely jointed chain level).<sup>8,19</sup>

$$\frac{\partial G(r, s)}{\partial s} = \frac{1}{6} \nabla_r G(r, s) - u(r, s) G(r, s) \quad (1)$$

which must be solved using the proper initial- and boundary conditions. Here  $G(r, s)$  is a so-called end-point distribution function and  $u(r, s)$  is the segment or self-consistent potential. We will not elaborate more on the details as we have used a lattice model variant of the Edwards equation, the model of Scheutjens and Fleer. These authors advocated a scheme wherein the space is discretized using a system of lattice layers  $r = 1, \dots, r_M$  in such a way that the segments of the molecules fit on the lattice sites. In each layer there are  $L(r)$  lattice sites. Here we focus on a spherical coordinate system for which the number of lattice sites grows quadratically, or more precisely:

$$L(r) = \frac{4}{3} \pi (r^3 - (r-1)^3) = 4\pi \left( r^2 - r + \frac{1}{3} \right) \quad (2)$$

and consider molecules of type  $i$  composed of  $s = 1, \dots, N_i$  segments. The particle ( $i = 0$ ) is composed of segments of type  $S$  and occupies coordinates  $r = 1, \dots, R$  completely, that is,  $\varphi_S(r) = 1$

$\forall r \leq R$ . Other molecules, necessarily, occupy lattice sites in the remainder of the layers. In the current system we have three monomeric molecules types: Water ( $i = 1$ ), cation  $\text{Na}^+$  ( $i = 2$ ) and anion  $\text{NO}_3^-$  ( $i = 3$ ). Hence  $N_1 = N_2 = N_3 = 1$ , and one or more polymeric species  $i = 4, \dots, I$  (here  $I > 4$  is used for the case of a polydisperse corona). Every polymer chain is constrained by segment  $s = 1$  to the surface of a particle core. Introducing  $\varphi_i(r, s)$  as the volume fraction of segment  $s$  of molecule  $i$  at coordinate  $r$ , the grafting constraint dictates that  $\varphi_{i>3}(r, 1) = 0 \forall r > R + 1$  and only  $\varphi_{i>3}(r, R + 1)$  has a finite value. Indeed the overall grafting density  $\sigma$ , that is the number of chains per particle, is given by:

$$\sigma = \sum_{i>3} \sigma_i = \sum_{i>3} L(r) \varphi_{i>3}(r, R + 1) \quad (3)$$

Note that all  $\sigma_{i>3}$  values are input quantities for the calculations.

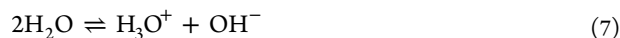
The radial volume fraction profiles  $\varphi_i(r, s)$  are the key “deliverables” of the SF-SCF modeling. The polymer chains typically are composed of neutral segments  $N$  and segments that contain one acid moiety,  $A$ . It is convenient to introduce the chain architecture operator  $\delta_{i,s}^X$ , which assumes the value unity when segment  $s$  of molecule  $i$  is of type  $X$  and zero otherwise. Obviously, all values for the chain architecture operator are specified by the input of the calculations. Using these we may compute various volume fraction distributions:

$$\varphi_i(r) = \sum_{s=1}^{N_i} \varphi_i(r, s) \quad (4)$$

$$\varphi_X(r) = \sum_i \sum_{s=1}^{N_i} \varphi_i(r, s) \delta_{i,s}^X \quad (5)$$

for the overall volume fraction profile per polymer chain type (or monomeric solvent), and the overall volume fraction profile of segment type  $X = W, \text{Na}, \text{NO}_3, N, A$ , respectively.

We are going to assume that the segments that incorporate an acid group can be found in one of two internal states, namely one which is uncharged  $\text{AH}$  ( $k = 1$ ) and one which is charged  $\text{A}^-$  ( $k = 2$ ). In addition the water monomer can occur in three possible states, namely in the neutral form representing  $\text{H}_2\text{O}$  ( $k = 1$ ), the protonated state  $\text{H}_3\text{O}^+$  ( $k = 2$ ) and deprotonated state  $\text{OH}^-$  ( $k = 3$ ). We refer to these internal states as  $A_k$  and  $W_k$ , respectively, where  $K = 1, \dots, K$  with  $K = 2, 3$  for  $A$  and  $W$  respectively, and  $K = 1$  for all other segment types. The internal states obey equilibrium conditions:



with equilibrium constants

$$K_a = \frac{[\text{A}^-][\text{H}_3\text{O}^+]}{[\text{AH}][\text{H}_2\text{O}]} = \frac{\alpha_{A2}\alpha_{W2}}{\alpha_{A1}\alpha_{W1}} \quad (8)$$

$$K_w = \frac{[\text{H}_3\text{O}^+][\text{OH}^-]}{[\text{H}_2\text{O}]^2} = \frac{\alpha_{W2}\alpha_{W3}}{\alpha_{W1}\alpha_{W1}} \quad (9)$$

where  $\alpha_{Xk}$  is the fraction of segments  $X$  in state  $k$ . The values of  $K_a$  and  $K_w$  are also input quantities. In principle the fractions may depend on the spatial coordinate, that is,  $\alpha_{Xk}(r)$ . So, it is possible to define yet another volume fraction distribution

$$\varphi_{Xk}(r) = \alpha_{Xk}(r) \varphi_X(r) \quad (10)$$

as the distribution of segments of type X in internal state  $k$ .

Conjugated to the segment distribution of eq 10 there are segment potentials which depend on the same variables:  $u_{Xk}(r)$ . Physically these potentials represent the work needed to bring a segment from the bulk (where the potentials are zero) to the coordinate  $r$ . This segment potential is composed of four contributions  $u_{Xk}(r) = u^{\text{sf}} + u_X^{\text{FH}} + u_{Xk}^{\text{el}} + u_X^{\text{po}}$ . From the subindex labels, we can see how various contributions depend on the segment type and/or internal state. We discuss these contributions (normalized by the thermal energy  $k_B T$ ):

- $u^{\text{sf}}(r)$  represents the work needed to make space for the segment at the coordinate  $r$ , relative to that in the bulk. The value is related to the compressibility constraint. More specifically the value is adjusted until all lattice sites are filled by segments or molecules:

$$\sum_X \varphi_X(r) = 1 \quad (11)$$

In practice we will increase the value of  $u^{\text{sf}}$  if the overall volume fraction of segments tends to go above unity and make its value smaller when there are still vacancies. The value of  $u^{\text{sf}}$  does not depend on the segment type, simply because we assume that all the segments have the same volume.

- $u_X^{\text{FH}}(r)$  represents the contribution that accounts for the short-range nearest-neighbor interactions in the system. We estimate the number of contacts using the Bragg–Williams approximation and use the well-known Flory–Huggins  $\chi_{XY} = (Z)/(2k_B T)[2U_{XY} - U_{XX} - U_{YY}]$  parameters to specify the cost in units of  $k_B T$  for a contact between segments of type X and Y, where  $U$  is the interaction energy for the indicated pair of segments, and  $Z$  is the lattice coordination number. From its definition it is clear that the like-contacts are chosen to be the reference and only unlike interaction may receive a nonzero  $\chi$  value. A positive value signals repulsion and a negative value mean attraction. For long polymers in monomeric solvent, the value  $\chi = 0.5$ , which is the theta-point, signals the border between good and poor solvents. Mathematically, we compute the Flory–Huggins contribution to the segment potential with

$$u_X^{\text{FH}} = \sum_Y \chi_{XY} (\langle \varphi_X(r) \rangle - \varphi_X^b) \quad (12)$$

Here the angular brackets represent a three-layer average

$$\begin{aligned} \langle \varphi(r) \rangle &= \lambda(r, r-1)\varphi(r-1) + \lambda(r, r)\varphi(r) \\ &+ \lambda(r, r+1)\varphi(r+1) \end{aligned} \quad (13)$$

wherein  $\lambda(r, r')$  is the *a priori* probability to “step” from layer  $r$  to a layer  $r'$ . From this definition it is clear that  $\sum_{r'=r-1, r, r+1} \lambda(r, r') = 1$ . Detailed balance considerations further require that  $L(r)\lambda(r, r+1) = L(r+1)\lambda(r+1, r)$ . This we can satisfy by choosing the transitions to depend on the contact area between layers  $r$  and  $r'$ .

$$\lambda(r, r+1) = \lambda \frac{4\pi r^2}{L(r)} \quad (14)$$

$$\lambda(r, r-1) = \lambda \frac{4\pi(r-1)^2}{L(r)} \quad (15)$$

The  $\lambda$  parameter is the *a priori* step probabilities in the limit  $r \rightarrow \infty$ .

Returning to the FH contribution to the segment potential (eq 12), we see that we have normalized the contribution using the bulk volume fractions  $\varphi_X^b$ . In passing we note that the bulk volume fractions obey the same compressibility relation as given in eq 11.

- $u_{Xk}^{\text{el}}(r)$  represents the electrostatic contribution. As all terms should be normalized to  $k_B T$ , we here write

$$u_{Xk}^{\text{el}}(r) = \frac{-e v_{Xk} \psi(r)}{k_B T} \quad (16)$$

wherein  $e$  is the elementary charge and  $v_{Xk}$  is the valency (including the sign) of the segment X in internal state  $k$ . The electrostatic potential  $\psi(r)$  is chosen such that the potential is zero in the limit of  $r \rightarrow \infty$  (bulk). In passing we note that the total number of charge  $q(r)$  at coordinate  $r$  can be evaluated as

$$q(r) = \sum_X \sum_k e v_{Xk} \varphi_{Xk}(r) L(r) \quad (17)$$

Furthermore, we allow for a local dielectric permittivity by implementing a simplistic way to make the permittivity depend on the local composition, in which we take the volume fraction average value

$$\varepsilon(r) = \varepsilon_0 \sum_X \varphi_X(r) \varepsilon_X \quad (18)$$

wherein  $\varepsilon_0$  is the dielectric permittivity for vacuum and  $\varepsilon_X$  is the relative dielectric permittivity of a phase composed purely by segments of type X.

Both the charge density and the dielectric permittivity profiles are needed to compute the electrostatic potential profile  $\psi(r)$ . The relevant Poisson equation is expressed in radial coordinates as

$$\frac{\partial}{\partial r} \left( L(r) \varepsilon(r) \frac{\partial \psi(r)}{\partial r} \right) = -q(r) \quad (19)$$

If  $\varepsilon(r)$  would have been constant, as is typically taken to be the case in the Poisson–Boltzmann (PB) theory, one can bring  $\varepsilon$  to the right-hand side of eq 19. Recalling that for sufficiently large  $r$  the number of sites at coordinate  $r$ ,  $L(r) \propto r^2$ , one may recognize the usual  $\nabla = 2/r(\partial)/(\partial r) + (\partial^2)/(\partial r^2)$ .

- $u_X^{\text{po}}(r)$  is a term due to the polarization that occurs when segments are placed in an electric field. In the classical PB theory this contribution is not included because the dielectric permittivity is kept constant. However, in our case the dielectric permittivity is spatially dependent and therefore this term is needed. To quantify this contribution, we need the electric field  $E(r) = -(\partial \psi(r))/(\partial r)$ . We realize that a segment of type X will have an induced dipole in this electric field which is proportional to  $\varepsilon_X E(r)$ . Further, the energy gain is proportional to the electric field and therefore

$$u_X^{\text{po}} = -\frac{1}{2} \varepsilon_0 (\varepsilon_X - 1) (E(r))^2 \quad (20)$$

where we choose to normalize this quantity such that in vacuum the contribution vanishes. The factor  $(1/2)$  is



needed because it can be shown that there is an entropy cost associated with the polarization and this cancels half the energy gain, so that only one-half is left. The values for the relative dielectric permittivities are input quantities that need specification.

The segment potentials are featured in the Edwards equation (eq 1). The mapping of this equation onto a lattice is well documented and leads to the so-called propagator formalism. For completeness we will also briefly discuss these here. Within this formalism one sees that the potentials are used to compute statistical weights in Boltzmann-like equations. Introducing the segment distribution function  $G_{Xk}(r) = \exp[-u_{Xk}(r)]$  as the statistical weight of finding a (free) segment of type  $X$  in state  $k$  at coordinate  $r$ , we can find the distribution of monomeric molecules composed of one  $X$  segment straightforwardly by

$$\varphi_X(r) = C_X G_X(r) = C_X \sum_k \alpha_{Xk}^b G_{Xk}(r) \quad (21)$$

where  $\alpha_{Xk}^b$  is the fraction of groups of type  $X$  in state  $k$  in the absence of an electrostatic potential, that is, if it is placed in the bulk. When there is just one state  $K = 1$ ,  $\alpha_{Xk}^b = 1$  obviously. In the case of water, we need  $\alpha_{W2}^b$  or  $\alpha_{W3}^b$  values as input. Indeed this input is equivalent to defining the pH in solution.  $C_X$  is a normalization factor which may be found by applying eq 21 for the bulk: when segment type  $X$  is exclusively present in one type of molecule  $C_X = \varphi_X^b$ . The overall volume fraction of  $X$  at coordinate  $r$  may be split up into the contributions of the states  $k$ :

$$\varphi_{Xk}(r) = \alpha_{Xk}(r) \varphi_X(r) = \frac{\alpha_{Xk}^b G_{Xk}(r)}{G_X(r)} \varphi_X(r) \quad (22)$$

Again, this equation is only used for computing the local proton and hydroxyl concentrations.

The polymer chains are composed of strings of segments  $S = 1, \dots, N$  and the segment type of each segment is known by the chain architecture operators. It is convenient to generalize the free segment distribution function accordingly

$$G_i(r, s) = \sum_X G_X(r) \delta_{i,s}^X \quad (23)$$

as these can be used in the propagator formalism. Introducing the end-point distribution function  $G_i(r, s|R+1, 1)$  as the statistical weight of finding segment  $s$  at coordinate  $r$  provided it is connected by a string of  $s-1$  segments to segment number  $s=1$  sitting at coordinate  $r=R+1$  and the complementary end-point distribution function  $G_i(r, s|N)$  as the statistical weight of finding segment  $s$  on coordinate  $r$  provided it is connected by  $N-s+1$  segments to segment  $s=N$  — which is not constraint and thus can be at many coordinates and therefore we do not specify it — we find the volume fraction distribution by the so-called composition law

$$\begin{aligned} \varphi_i(r, s) &= C_i G_i(r, s|R+1; N) \\ &= \frac{G_i(r, s|R+1, 1) G_i(r, s|N)}{G_i(r, s)} \end{aligned} \quad (24)$$

Here again  $C_i$  is a normalization constant which forces the distribution to be consistent with the grafting density:

$$\sum_r \varphi_i(r, s) L(r) = \sigma_i \quad (25)$$

and thus  $C_i = \sigma_i / \sum_r L(r) G_i(r, s|R+1; N)$ . The nominator of the latter equation may be identified as the chain partition function.

In eq 24, we see that the volume fractions follow from the product of the two complementary end-point distribution functions. The normalization is to ensure that the statistical weight for segment  $s$  is counted just once. One can only verify this statement by inspecting the two propagators used to generate the end-point distributions:

$$\begin{aligned} G_i(r, s|R+1, 1) \\ = G_i(r, s) \sum_{r'=r-1, r, r+1} \lambda(r, r') G_i(r', s-1|R+1, 1) \end{aligned} \quad (26)$$

$$G_i(r, s|N) = G_i(r, s) \sum_{r'=r-1, r, r+1} \lambda(r, r') G_i(r', s+1|N) \quad (27)$$

which are initiated by  $G_i(r, 1|R+1, 1) = G_i(r, 1) \delta_{r, R+1}$  where this  $\delta$  equals unity when  $r = R+1$  and zero otherwise, and by  $G_i(r, 1|N) = G_i(r, N)$ , respectively.

In summary, the SF-SCF machinery specifies how to obtain the various volume fraction profiles once the segment potentials are known. It also specifies how to obtain the segment potentials when all volume fraction profiles are known. A fixed point of these equations, usually referred to as the self-consistent field solution, is routinely found using a quasi-Newton iteration scheme. Typically the accuracy in these calculations is seven significant digits.

## MODEL PARAMETERS

To specify the molecular model used, we will need to give details about the lattice parameters, the monomeric parameters, and the molecular details. We will discuss these, mentioning the default parameter set. Values for this set were found from a rough fitting of some experimental findings for the core-shell particles.

**Lattice Parameters.** As explained above, we have used a lattice with spherical geometry. Typically the number of lattice layers was  $M = 300$ . This value is sufficiently large so that all density gradients have relaxed to the bulk value. We have used a simple cubic lattice, that is,  $\lambda = 1/6$ . In the Scheutjens-Fleer method the bond length between segments in the chain is equal to the characteristic size of the lattice  $b$ . Consistent with the statistical segments used to describe the chain we have implemented  $b = 0.6$  nm. Using this value, we estimated the conversion from a monomeric volume fraction to a molar concentration. The conversion factor is close to 10.

The first layer of the lattice was placed with an offset of  $R_{\text{core}} = 70$  layers from the center of the particle core, consistent with the experimentally determined radius of the particle core, which was found to be 42.5 nm.

**Monomer Parameters.** We have chosen to have two types of water molecules. The majority of the solvent (90%) is a water molecule which does not dissociate ( $W$ ). The second component (10%), referred as  $W_i$ , is the same water molecule but subject to the autodissociation equilibrium reaction (eq 7), with a dissociation constant shown in eq 9 set to  $\text{p}K_w = 14$ . One motivation to do this is that we can simply relate the proton volume fraction in terms of volume fractions equal to the molar concentration, considering that the discretization length is  $b = 0.6$  nm and consequently the conversion of monomer volume fraction to molar concentration is a factor of 10. The two water types are indistinguishable with respect to dielectric permittivity and interaction parameters with the other components. In each calculation one needs to specify the pH. This is done by

specifying the degree of dissociation of (the minority component of) water in the bulk, that is  $\text{pH} = -\log(\alpha_{\text{W}2}^b)$ .

The 1:1 electrolyte was represented by two monomeric species, named Na (valence +1) and  $\text{NO}_3$  (valence −1). Apart from the valence, the ions are expected to have the same properties as water, that is, they share the same dielectric permittivity and FH  $\chi$  parameters with water molecules. This is an approximation of course, but this pragmatic choice minimizes the number of parameters in the model.

As explained in the Introduction, formally the FH  $\chi$  parameter is inversely proportional to the temperature  $T$ . However, this dependence fails dramatically, especially for polymers with a LCST. The solution for this is to consider the FH  $\chi$  parameter to be a free energy parameter which contains both an enthalpic and an entropic contribution

$$\chi(T) = A + \frac{B}{T} \quad (28)$$

This, in fact, doubles the number of interaction parameters. It is not trivial to find estimates for the values of  $A$  and  $B$ . Below we used the values  $A = 10.6$  and  $B = -3000$ , which resulted from our attempts to reproduce the experimentally found height of the brush (size of the particle shell) as a function of the temperature  $T$ . The exact criteria used for this fitting will be evaluated in the Discussion.

As discussed below, the layer of grafted chains consists of molecules that are composed of various segment types. The first segment of the chain, which is the grafting segment, is here referred to segment X. For analysis purposes, we introduce a probe segment at the free end of the chains which we will refer to as segment G. In between these two segments, we have a chain composed of neutral segments N and chargeable segments A that can be in two internal states. The internal states obey the dissociation equilibrium reaction shown in eq 6 and the reaction constant shown in eq 8 is given by  $\text{p}K_a = 4.66$ , consistent with literature reports.<sup>7</sup>

With respect to the interaction parameters we are going to assume that the solvent quality is homogeneous along the chain. That is, the segments X, N, A, G are interacting with water with the interaction parameter  $\chi_{\text{W}}$ . Below we will discuss how we are going to vary this parameter to mimic the change in temperature in the system. The dielectric permittivity of the segments is set to  $\epsilon_r = 2$  for N, G and  $\epsilon_r = 3$  for A (irrespective of which internal state the segment is in). All other components have  $\epsilon_r = 80$ .

We note that the electrostatic contribution in the segment potential is also temperature dependent. We have not implemented the change in temperature for this contribution, that is, we kept for this term  $T$  constant and equal to room temperature. This is consistent with the Ansatz that we also ignored the temperature dependence of the dielectric permittivity. We believe these two dependences largely compensate each other.

The core of the particles is taken to be composed of monomers of type S. The dielectric permittivity of this phase is set to  $\epsilon_s = 3$ , mimicking a hydrophobic domain of PMMA. In principle it is necessary to specify the disparity of interaction of water molecules and polymer segments for the surface groups.

To prevent the development of a strong depletion zone near the surface, it was necessary to consider a repulsive interaction between the water segments and the surface (similar to an attraction of all other components). This is also consistent with the PMMA core being hydrophobic. We used  $\chi_s = 1$  for the interaction of water W and Wi segments with the surface, where

it should be understood that the interaction of the polymer segments with the surface is the reference state for this interaction (the  $\chi$  of polymer segments X, N, A and G with S is set to zero).

**Molecule Parameters.** From the synthetic protocol (see Materials and Methods), it is expected that there is a ratio of 11.8 NIPAM monomers per MA monomer in the shell of the particles. As mentioned already, we have chosen to use statistical segments. More specifically we used segments composed of two monomers each. Segment A is composed of one acid monomer and one NIPAM monomer, and segment N is composed of two NIPAM monomers. The experimental composition thus translates into an average composition of 5 N per A segment. In the default case we consider molecules that have acid segments homogeneously distributed along the chains of the brush, corresponding to the structure  $X_1(N_5A_1)_nG_1$ . Here the value for  $n$  determines the overall chain length  $N = (6n+2)$ . In the default system all chains are equally long.

The second parameter that is needed is the grafting density  $\sigma$  (number of chains per particle). Together with the value of  $N$ , it determines the amount of polymer  $\theta$  in the corona layer. More specifically  $\theta = \sigma \times N = \sigma \times (6n+2)$ . At high temperatures and at low pH the corona layer is collapsed (as shown in Figure 1, case

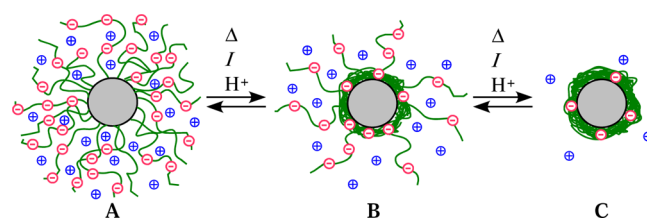


**Figure 1.** Schematic of the volume phase transition of P(N-MA) particles with a core–corona structure. The volume change of the corona is triggered by changes in temperature, pH or ionic strength. The acid groups along the PNIPAM chains are indicated by  $\ominus$ , and the mobile counterions by  $\oplus$ . Key: (A) the expanded state; (B) the transition state; (C) the collapsed state. Near the transition point the brush can be in a microsegregated state, that is, most of the corona chains have collapsed in a dense region near the core (typical for the high  $T$  state) while a few remaining chains which are more charged are strongly stretched and solvated (low  $T$  state).

C). The size of the particles in this limit is given by  $R_{\text{tot}} = R_{\text{core}} + R_{\text{corona}}$ . Knowing the core size, we can estimate the thickness of the corona layer in the collapsed state. In the model, this thickness is estimated by  $R_{\text{corona}} = d\theta/(4\pi R_{\text{core}}^2)$ . Comparison with experimental data thus gives an estimate for  $\theta$ , which in the default system is  $\theta = 3 \times 10^5$ . The remaining issue is to find a reasonable estimate for the length of the chains, that is, a value for  $n$ . At low temperatures, high pH and low ionic strengths, the chains in the corona are strongly hydrated (as shown in Figure 1, case A). The electrostatic interactions force the chains to stretch strongly away from the core. The height of the corona layer (which is experimentally accessible) can be reasonably well reproduced by taking a value of  $n = 80$  ( $N \approx 500$ ). This means that the default system has  $\sigma \approx 600$  chains per particle. In the discussion we will also mention results for which the charged groups are distributed unevenly over the chains. We also discuss the case when the chains are of unequal length. As these results will not be extensively analyzed, we will specify the details when the calculations are discussed.

## MATERIALS AND METHODS

**Synthesis of Stimuli-Responsive Core–Shell Nanoparticles.** The negatively charged polymer nanoparticles with a PMMA core and a shell of PNIPAM and poly(methacrylic acid), p(N-MA), were prepared by a two-stage shot emulsion copolymerization technique in water, using the monomers methyl methacrylate (MMA, from Aldrich, 99%, distilled under vacuum), *N*-isopropylacrylamide (NIPAM, from Acros, 99%, recrystallized in hexane), and methacrylic acid (MA, from Aldrich, 99%, distilled under vacuum). The initiator was potassium persulfate (KPS, from Aldrich, 99% ACS reagent, used as received), and the surfactant was sodium dodecyl sulfate (SDS, from Sigma, 99% GC grade, used as received).

In the first step, the PMMA core was prepared by batch emulsion polymerization from a mixture of SDS (0.1 g/100 g of mixture, ca. 3.8 mM—a concentration below its critical micelle concentration,  $\text{cmc} \approx 8 \text{ mM}^{20}$ ), KPS (0.0501 g) and MMA (5 mL, 4.7 g) in Milli-Q water (50 mL). The mixture was kept at 70 °C, under nitrogen, until ca. 80% conversion was reached. Then, in the second stage, a mixture of 1.01 g of NIPAM and 0.065 g of MA was added in three shots, 10 min apart, to the reaction medium at 70 °C, to form the shell around the PMMA core. The mixture was allowed to react for another 2 h to obtain a final conversion of 100%. The solids content of the final particle dispersion (gravimetric analysis) was 9.0%. The polymerization conversion was determined from the ratio of the experimentally determined solid content and the solid content calculated for complete polymerization. Absence of the characteristically invasive NIPAM smell at the end of polymerization provided immediate (though qualitative) confirmation of 100% NIPAM conversion.

The addition of NIPAM over a time interval starting before the complete conversion of MMA favors the formation of monodisperse particles with smooth shells covering the entire PMMA core and avoids the nucleation of PNIPAM aggregates in the water phase.<sup>21</sup> The initiation of PNIPAM does not take place in the aqueous phase because, although the initiator is water-soluble, NIPAM is only added to the reaction mixture when the conversion of PMMA is already ca. 80%, and so both NIPAM and MA react preferably at the particle surface where PMMA oligo-radicals are still active.

**Sample Preparation.** The particle dispersion was diluted to half its original solid content with Milli-Q water and cleaned by dialysis (Spectra/Por membrane, MWCO 6–8000 kDa) changing water twice a day during two weeks in order to remove all traces of surfactant. The ionic strength was adjusted using a NaNO<sub>3</sub> solution prepared from solid NaNO<sub>3</sub> (Merck, suprapur). The pH was adjusted using 1 mM buffer (MES for pH between 5.0 and 6.5 and MOPS for pH > 6.5). Stock solutions of MES (2-(*N*-morpholino)ethanesulfonic acid) and MOPS (3-(*N*-morpholino)propanesulfonic acid) buffers were prepared from the solids (Fluka, Microselect, > 99.5%). Solutions prepared from HNO<sub>3</sub> (Merck, Suprapur) and NaOH (0.1 M standard, Merck) were used to adjust the pH. The pH measurements were performed using a Denver Instruments semimicro combined pH electrode (300736–1) connected to a HANNA pH 211 meter.

**Particle Size and Size Distribution.** The hydrodynamic radius of the nanoparticles ( $R_h$ ) was determined by dynamic light scattering using an ALV apparatus with an Ar-ion laser (Cobolt Samba 300 mW at 532 nm). Diluted particle dispersions (5.0 × 10<sup>−3</sup> wt % of nanoparticles) were measured at 90° and the intensity fluctuations were analyzed automatically with an ALV-

7002 digital correlator. The temperature was controlled (±0.1 °C) using an Haake Phoenix-II heater/circulator with a C30P cooling bath, with Haake Sil 180 mineral oil. The temperature was read directly from the decalin bath using a Platinum Pt100 temperature sensor. Each hydrodynamic radius determination was calculated from at least 30 autocorrelation curves.

The hydrodynamic radius of the glassy PMMA core,  $R_c = (42 \pm 1) \text{ nm}$ , was measured by DLS of model PMMA nanoparticles synthesized in similar conditions as those used to prepare the core of the core–shell particles, and does not change in the interval of temperature, pH and ionic strength used. This size was also found in SEM images of the dry particles.<sup>7</sup>

**Potentiometric Titrations. Equipment.** The potentiometric measurements were performed using a Mettler-Toledo T90 system with four 1 mL autoburettes (20000 steps, minimum volume addition 0.05 μL) (buret 1, HNO<sub>3</sub>; buret 2, NaOH; buret 3, NaNO<sub>3</sub>; buret 4, H<sub>2</sub>O) and a Mettler-Toledo pH glass combined electrode DGi102 mini. The system was constantly under nitrogen purging. Mettler-Toledo LabX titration software was used to control the apparatus.

**Reagents.** Nitric acid 0.1 M, p.a., Riedel-de Haën; sodium hydroxide 0.1 M, p.a., Merck; sodium nitrate p.a., Merck; P(N-MA), Barnstead type II ultrapure water, standard pH buffers pH 4, 5, 6, and 7, Merck; sodium tetraborate decahydrate, p.a., Fluka.

**Methodology. Standardization of HNO<sub>3</sub> and NaOH.** The HNO<sub>3</sub> was standardized by five volumetric titrations against sodium tetraborate decahydrate, yielding a concentration of  $0.0980 \pm 0.060 \text{ mol} \cdot \text{L}^{-1}$  and the NaOH was standardized by eight titrations with HNO<sub>3</sub>, yielding a concentration of  $0.0976 \pm 0.006 \text{ mol} \cdot \text{L}^{-1}$  both at 95% confidence levels.

**pH Electrode Calibrations.** The pH electrode was calibrated in duplicate before each titration first using the four pH buffer standards (4.0, 5.0, 6.0, and 7.01) to verify that it was working properly.

**Titration Procedures.** All potential readings were performed using a drift of 0.100 mV/min or a time limit of 5 min. The samples were initially degassed for 5 min using nitrogen 99.99% pure, and then kept under pressure for the duration of the experiment. The titrations were carried out at  $23.0 \pm 0.5 \text{ °C}$  in a temperature controlled room. Titrations were performed using three different ionic strengths (0.003; 0.015 and 0.100 mol·L<sup>−1</sup>).

**Blank titration:** The blank subtraction procedure was applied in these titrations. To obtain the blank values the pH was initially set to the value of 3.0 by addition 0.135 mL of HNO<sub>3</sub> from buret 1 to 20 mL of NaNO<sub>3</sub> 0.003 mol·L<sup>−1</sup> (19.950 mL of H<sub>2</sub>O and 0.050 mL of NaNO<sub>3</sub> 1 mol·L<sup>−1</sup>). After the initial reading stabilized ( $\approx 220 \text{ mV}$ ), the solution was titrated to pH 11 ( $\approx -190 \text{ mV}$ ) by successive additions of 5 μL of NaOH and back to pH 3.5 ( $\approx 205 \text{ mV}$ ) by successive additions of 5 μL of HNO<sub>3</sub>. For the second and third back and forth blank titration the procedure was repeated with the initial additions of 0.260 and 1.800 mL of NaNO<sub>3</sub> 1 mol·L<sup>−1</sup> to set the ionic strength at 0.015 and 0.100 mol·L<sup>−1</sup> respectively.

**P(N-MA) titration:** For the P(N-MA) titration the procedure was exactly the same as described for the blank titration except that the initial solution is a 20 mL solution containing 0.15% (w/w) P(N-MA) in NaNO<sub>3</sub> 0.003 mol·L<sup>−1</sup>. The blanks are subtracted from the titrations curves to obtain the charge vs pH dependence of the P(N-MA).

## RESULTS

We know from the synthesis that we have core–shell particles for which the typical size of the corona is in the same order of



magnitude as the core size. This means that these particles are typically in between the limiting situation of the star-like polymer brush and the quasi-planar one. For these intermediate situations analytical estimates are known to be not very accurate and numerical SCF solutions should be used to obtain the required information.

Hydrophobic polyelectrolyte brushes have a rich behavior because the structure of the brush is a function of the temperature (solvent quality), the pH and the ionic strength. In the following, we will first give an overview of the properties in a “case study” for systems near the default parameter setting. In the second part of the Results, we will show how the theoretical predictions compare to experimental data. To judge the origin of the observed differences, we briefly consider more complex models of the corona layer in the third part of the results, which sets the stage for the discussion.

**Case Study.** Since the core of the particles is in a glassy state, we focus on the properties of the polymer brush which composes the corona. The properties of this corona are illustrated by specifying a “default” system taken to be in a regime aiming to represent the system around the transition temperature, 306 K (33 °C, represented in Figure 1, case B). For significantly lower temperatures, it is believed that the brush is hydrated and swollen (Figure 1, case A). At higher temperatures the brush is collapsed in a dense layer (Figure 1, case C). Hence in this case study we will focus on the properties of this default system and consider what happens when the temperature, the pH or ionic strength is varied in a relevant range.

As explained in the parameter section the brush chains were modeled with an homogeneous acid segment distribution along the chain, a total chain length  $N \approx 500$  segments and a total amount of segments per particle  $\theta = 3 \times 10^5$ . The sequence of segments was  $X_1(N_5A_1)_{80}G_1$ .

In Figure 2a, we present the radial volume fraction profiles of the brush at pH 5.0, ionic strength  $I = 15$  mM and  $\chi_{WN} = 0.8$ , which corresponds by our calibration to a temperature  $T \approx 306$  K, as a function of the distance to the core  $\Delta r \equiv (r - R_{\text{core}})$  in nm.

In these conditions, we observe a microphase segregated structure with most of the brush in a condensed high-density phase, and a small fraction in an expanded low-density phase. This can be seen in plot a of Figure 2. In this plot, we present the radial profiles of the volume fraction  $\phi$  of both the brush polymer chains (straight lines) and the end points of the brush polymer chains, segments G (dashed lines). Upon close inspection we see that the end-point distribution is bimodal (there are two maxima in the profile). This indicates that there are two chain populations, with most chains fully collapsed, and a small fraction completely expanded. Indeed, end-grafted chains do not assume in between conformations for which a part is condensed and the remainder expanded. The idea is that a large number of chains collapse to give the remainder of the chains space to expand. For such microphase-segregated brush, it is not easy to quantify the experimentally accessible height of the brush. Here, we present several possibilities of measuring the brush height of our particles. Since most of the polymer is in the condensed phase, the first and second moments of both the polymer distribution (i and ii) and the end segments G distribution (iii and iv) point to this region. However, in the case of the DLS measurements, the hydrodynamic radius should depend mostly on the small part of the brush that is stretched out, and that is not taken into account by these measures. To overcome this, we measured the distance at which the volume fraction  $\phi$  of the polymer reaches a threshold value of 0.001 (v), that we consider

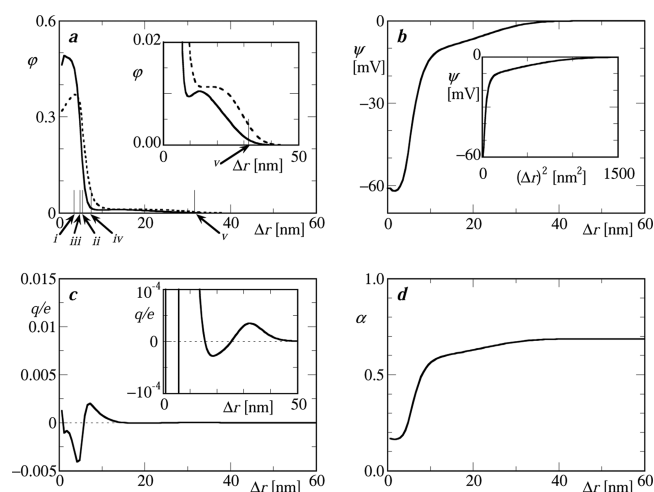


**Figure 2.** Radial profiles of the brush of the nanoparticles at pH = 5.0, ionic strength  $I = 15$  mM and  $\chi_{WN} = 0.8$  as a function of the distance to the core  $\Delta r \equiv (r - R_{\text{core}})$  in nm. (a) volume fraction  $\phi$  profiles. Continuous line: polymer; dashed line: end segments G (multiplied by 500); thin vertical lines: brush height as given by (i) the first and (ii) second moments of the polymer distribution; (iii) the first and (iv) second moment of the end segments distribution; (v) the polymer distribution reaching volume fraction  $\phi = 0.001$ . Inset: Expansion of the profile focusing on the dilute regions. (b) Electrostatic potential  $\psi$  in mV. Inset: potential as a function of  $(\Delta r)^2$ , showing a parabolic dependence of the electrostatic potential on the distance to the core. (c) Charge density  $q/e$ . (d) Degree of ionization  $\alpha$ .

to be a better measure of the hydrodynamic radius, even though the threshold value (0.001) is arbitrarily chosen.

In Figure 1b, we present the radial profile of the potential  $\psi$  as a function of the distance to the core  $\Delta r$  in nm. We can see that the potential is much more negative near the core of the particles, due to the charges in the condensed phase. However, the charges in the small amount of stretched brush in the expanded phase region still significantly contribute to the potential. In this plot, we also present as an inset the radial profile of the potential  $\psi$  as a function of the square of the distance to the core  $(\Delta r)^2$  in nm<sup>2</sup>. We can see that the potential shows a linear dependence with the square of the distance to the core. This parabolic dependence on the potential with the distance to the core is predicted by analytical theory.<sup>22</sup>

In Figure 2c, we present the radial profile of the charge density. As expected, most of the (uncompensated) charges are near the core, since most of the polymer is in the condensed phase. However, we can still see a residual charge along the chains in the expanded phase, up to about 40 nm. By inspection of the radial charge distribution, it is noticed that the local charge is extremely low, that is, much lower than the “proton” charge along the polyelectrolyte chain. This observation has been noticed before and is at the basis of the local electroneutrality approximation (LEA) often used in analytical theory.<sup>23</sup> Indeed, the counterions come into the brush and locally compensate the charge of the polymers. Such an effect is well-known and in gels leads to the Donnan potential.

In Figure 2d, we present the radial profile of the degree of ionization. A relatively low degree of ionization is found near the core. This suppression of the ionization is due to the strong negative potential that prevent the ionization in this region, comparing to the expanded phase where the potential is much less negative. The degree of dissociation  $\alpha(r)$  approaches  $\alpha^b$  at



the periphery of the corona. The bulk dissociation is controlled only by the difference between pH and  $pK_a$ .

In Figure 3 we can see how the radial density profiles of the brush depend on  $\chi_{WN}$ , which is related to temperature  $T$  (plot a),

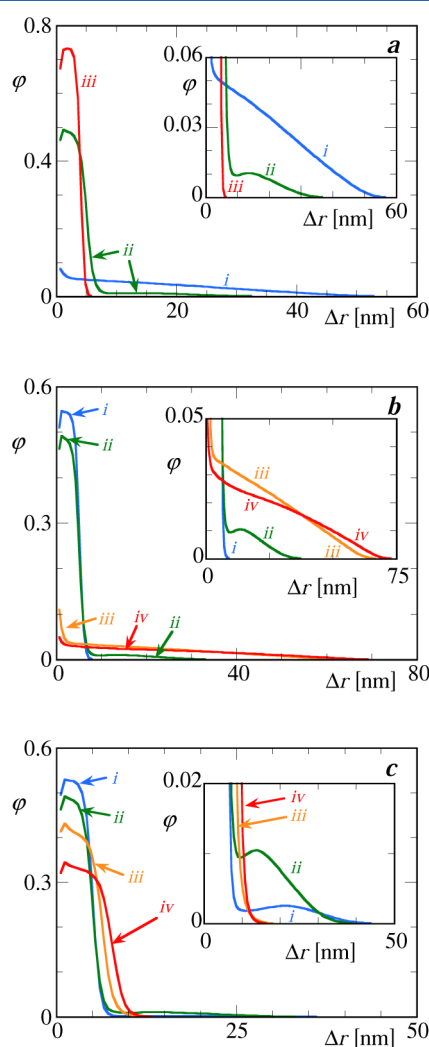


**Figure 3.** Radial volume fraction profiles of the brush as a function of the distance to the core  $\Delta r$  in nm. (a) At pH = 5.0, ionic strength  $I = 15$  mM,  $\chi_{WN} = 0.2$  (i), 0.8 (ii), 1.2 (iii), corresponding to temperatures  $T$  of about 288, 306, and 318 K, respectively. (b) At ionic strength  $I = 15$  mM and  $\lambda_{WN} = 0.8$ , pH = 4.0 (i), 5.0 (ii), 6.0 (iii), 7.5 (iv). (c) At  $\chi_{WN} = 0.8$ , pH = 5.0, ionic strengths  $I = 3$  mM (i), 15 mM (ii), 100 mM (iii), 1000 mM (iv). Insets: Expanded scale on the y-axis.

pH (plot b), and ionic strength  $I$  (plot c). These profiles should provide an insight into the responsiveness of the brush to various control parameters.

In Figure 3a, we show the brush density profiles at pH = 5.0 and at ionic strength  $I = 15$  mM, at  $\chi_{WN} = 0.2$  (i), 0.8 (ii), and 1.2 (iii), which should correspond to a temperature  $T$  of about 288, 306, and 318 K, respectively. Since PNIPAM, the major constituent of the shell, has a LCST behavior, as we increase the temperature, the affinity to water will decrease, and consequently a volume phase transition (VPT) should occur with a collapse of the shell over the core. At the lowest temperature (i,  $\chi_{WN} = 0.2$ ), the N segments (corresponding to 2 NIPAM monomers) have the greatest affinity to the solvent and the system is completely in the expanded phase. At the

intermediate temperature (ii,  $\chi_{WN} = 0.8$ ), the system is partially collapsed due to the decreasing of the affinity between N and water segments, being in the conditions of Figure 2. If we continue to increase the temperature (iii,  $\chi_{WN} = 1.2$ ), the affinity between N segments and water will continue to decrease and the system will become fully collapsed.

In Figure 3b, we present the profiles at ionic strength  $I = 15$  mM and  $\chi_{WN} = 0.8$ , at pH = 4.0 (i), 5.0 (ii), 6.0 (iii), and 7.5 (iv). At pH = 4.0, the polymer is completely collapsed, but as we increase the pH (pH = 5.0), we have once again the microphase segregated structure previously seen in Figure 2. As we continue to increase the pH and have more charge in the system due to ionization, all of the brush enters in the expanded state due to charge repulsion.

In Figure 3c, we show the profiles also at  $\chi_{WN} = 0.8$ , with pH = 5.0 and ionic strengths  $I = 3$  (i), 15 (ii), 100 (iii), and 1000 mM (iv). At the lowest ionic strengths, the system presents a microphase segregated structure. As we increase the ionic strength, the system collapses completely and the expanded phase is no longer seen, due to the screening of the charges in the acid segments by the salt, and consequent diminishing of the electrostatic repulsion.

In parts a and b of Figure 4, we can see how the brush height  $H$  and the degree of ionization  $\alpha$  vary with pH, at ionic strength  $I =$

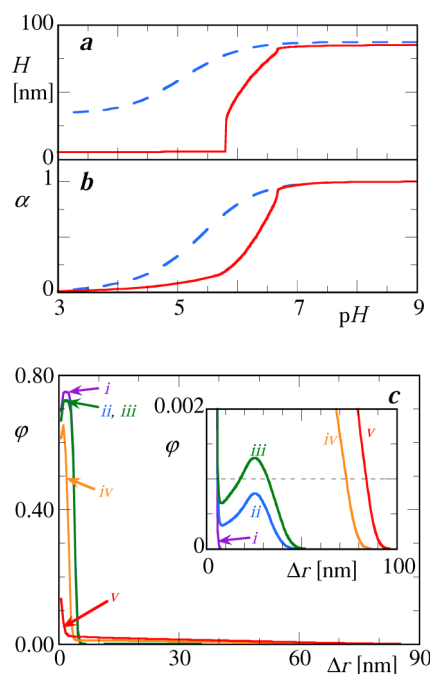


**Figure 4.** (a) Height  $H$  and (b) degree of dissociation  $\alpha$  as a function of pH at ionic strength  $I = 3$  mM. Blue dashed line:  $\chi_{WN} = 0.2$ . Red solid line:  $\chi_{WN} = 1.2$ . (c) Radial volume fraction profiles in the transition region at pH 5–7 and  $\chi_{WN} = 1.2$  as a function of the distance to the core in nm. Inset: expansion on the y-axis, showing the threshold value  $\phi = 0.001$  at which the height is determined.

3 mM and  $\chi_{WN} = 0.2$  and 1.2, corresponding to temperatures  $T \approx 288$  and 318 K, respectively. As expected, we see an increase of  $H$  and  $\alpha$  as we increase the pH. In Figure 4c we can see the profiles in the proximity of the transition pH region. At pH = 5.0 (i), the brush is completely in the collapsed state. At pH = 5.77 (ii), we can see the presence of a small fraction in an expanded state. However, the volume fraction  $\phi$  is still below the defined threshold (0.001), and therefore height is given by the collapsed

region as about 6 nm. At pH = 5.83 (iii), the volume fraction  $\varphi$  is now over the threshold and height is calculated as 32 nm. The apparent sudden jump in height at pH  $\approx$  5.8 is due to the reaching of the aforementioned threshold value. Above this, the brush height increases gradually (iv) until complete ionization at pH  $\approx$  6.8 and upward (v).

**Comparison with Experimental Data. Dynamic Light Scattering.** We have characterized the behavior of our particles by DLS, at several temperatures, pH and ionic strengths.

Since by DLS we obtain the hydrodynamic radius of the particles, in order to compare with the brush heights obtained from the model, we have calculated  $\Delta_r$ , that is the difference of the hydrodynamic radii of the particles  $H$  and the hydrodynamic radius of the core, measured also by DLS before the shell polymerization step as  $R_{\text{core}} = 42.5$  nm, as previously mentioned in the Model Parameters.

We begin with homogeneously distributed sequences of segments with five N segments per each A segment, at pH 4.0, in order to minimize the charges of the brush, and fitted the higher temperatures DLS data (312–318 K) with model data obtained at  $\chi_{\text{WN}}$  values between 1.0 and 1.2, at ionic strengths  $I = 3$  and 15 mM, considering that in both cases the particles would be in a completely collapsed state, and all of the height would correspond to brush segments. We tried several values for the total number of brush segments  $\theta$  and obtained the best fit for a value of  $\theta = 3 \times 10^5$ . We then tried to fit with several chain lengths, and reached our best global fittings, considering all the ionic strengths and with more attention to the lower temperature or  $\chi_{\text{WN}}$  regions, with the sequence of segments for the brush that was previously described,  $X_1(N_5A_1)_{80}G_1$ .

From these fittings we also calibrated the correspondence of the  $\chi_{\text{WN}}$  to the temperature  $T$  in K, having obtained the parameters previously described in the Model Parameters.

The experimental data, together with the model curves with which we obtained the best global fittings, can be seen in Figure 5.

The model curves follow semiquantitatively the experimental data. While the fitting is not perfect, we can consider that, in general, the trend for the evolution of shell height with the temperature in the model follows that of the experimental data. The deviations from experimental data, however, tell us also that there are aspects that are not yet properly taken into account in the model. Alternatively, there are theoretical shortcomings that can be targeted to the mean field approximation.

**Potentiometric Data.** We have also performed potentiometric measurements with our particles and we present these in comparison with the corresponding modeling curves in Figure 6. In this figure we present the degree of dissociation as a function of the pH of the system. We can see that the “titration” curves show a less pronounced slope, that is a slower variation of the charge over a wider pH range, than the modeling curves. Recalling the intrinsic  $pK_a = 4.66$ , the SCF calculations indicate just a modest polyelectrolyte effect at room temperature: there is a shift of the “effective”  $pK_a$  of about 1 pH unit. This limited shift is attributed to the fact that the chains are not extremely densely charged. Moreover, as long as the chains are radially extended (when the brush is in the expanded state) the distance between the charges is not small compared to the Debye length and therefore the polyelectrolyte effect in the model is limited. Experimentally a truly pronounced shift of the effective  $pK_a$  is found. Possibly this indicates that the value of the intrinsic  $pK_a$  is higher than anticipated. From a modeling point of view, large values of the effective  $pK_a$  can only be found for collapsed PE

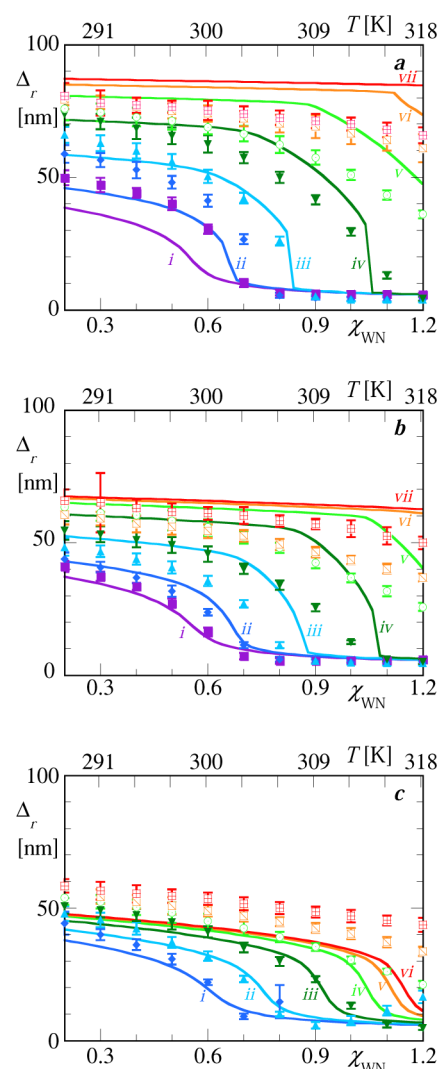


**Figure 5.** Modeled curves compared with the experimental DLS data. Brush height  $H$ , as a function of the Flory–Huggins solvent quality parameter  $\chi_{\text{WN}}$ , as found by the classical SCF theory, with total brush segments parameter  $\theta = 3 \times 10^5$ , compared to experimental DLS results, calculated from the difference between the hydrodynamic radii of the particle and of the core, at pH 4.0 (violet ■), 4.5 (blue ◆), 5.0 (light blue ▲), 5.5 (green ▼), 6.0 (green ○), 6.5 (orange □) and 7.5 (red ▢), as a function of the temperature. (a) Ionic strength  $I = 3$  mM at pH 4.0 (i), 4.5 (ii), 5.0 (iii), 5.5 (iv), 6.0 (v), 6.5 (vi), and 7.5 (vii); (b)  $I = 15$  mM at pH 4.0 (i), 4.5 (ii), 5.0 (iii), 5.5 (iv), 6.0 (v), 6.5 (vi), and 7.5 (vii); (c)  $I = 100$  mM at pH 4.5 (i), 5.0 (ii), 5.5 (iii), 6.0 (iv), 6.5 (v) and 7.5 (vi).

brushes, cf. Figure 4b. We may argue that experimentally there is a range of  $pK_a$  values pointing to some sort of heterogeneity in environments of the acid groups which is not accounted for the model. The inability of the theory to predict a strong shift of the titration curve at room temperature might therefore point to the option that at room temperature the PNIPAM brush is already in a microsegregated state wherein part of the carboxylic acid groups can be in hydrophobic pockets. Such nonideal state of the brush at room temperature has not been assumed in the parametrization of the model (yet).

Even though such nonideal behavior of the PNIPAM brush at room temperature is a viable hypothesis, it is of interest to consider other variations of the model to explain the observed deviations. These alterations of the model will be presented next.

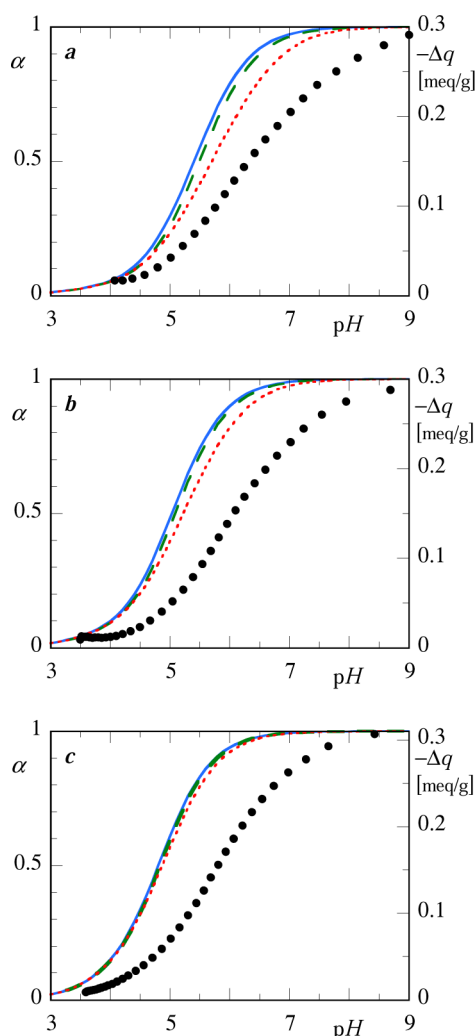


**Figure 6.** Degree of ionization  $\alpha$  at  $\chi_{WN} = 0.5$  as a function of pH (left ordinate); the differential charge per gram of particles measured by potentiometry at 23 °C (right ordinate: closed spheres). Blue solid lines: default system (A segments homogeneously distributed along the chain). Green dashed lines: inhomogeneously charged brush. Red dotted lines: polydisperse brush. (a) Ionic strength  $I = 3$  mM; (b)  $I = 15$  mM; (c)  $I = 100$  mM.

**Alternative Models.** So far, we have only presented results with homogeneously distributed chains with five N segments between each A segment. However, in the polymerization reaction it is known that methacrylic acid monomers are more reactive than NIPAM. So, it is expectable that there might be a higher amount of acid monomers relatively to NIPAM monomers near the core; hence, we may have a lower number of N segments per each A segment near the grafting segment X, and the opposite when moving away from it. This difference might have been suppressed by the addition of methacrylic acid in three steps during the synthesis, instead of adding it all at once in the beginning of the polymerization reaction (see Experimental Section). Nevertheless it is useful to probe how sensitive the brush properties are with respect to the way the charge is distributed.

Let us therefore consider the so-called inhomogeneously charged brush, implemented by a brush composed of chains wherein the charge density of the chains is higher near the grafting segment and lower near the free end. More specifically we generated results for a brush composed of

$X_1(N_2A_1)_{20}(N_4A_1)_{20}(N_6A_1)_{20}(N_8A_1)_{20}G_1$  chains. These chains have approximately the same length as the chains used in the default system and we implemented the same grafting density. One of the complications that was found for this system is that the collapsed brush did not wet the corona properly and a water layer between the particle core and the collapsed polymer layer developed. This was counteracted by implementing a repulsive interaction between the particle core and water,  $\chi_{WIS} = \chi_{WS} = 1.0$ . We note that this parameter (repulsion of water from the core) is consistent with the fact that poly(methyl methacrylate) (the material in the core) is relatively hydrophobic.

A small selection of the results for the inhomogeneously charged brush (dashed curve) can be seen in Figure 6, in comparison with the default system (solid curve), the case of a polydisperse brush (dotted curve) to be presented below and experimental results (closed spheres). The effect of the inhomogeneous distribution of the charges is small. Close inspection proves that the inhomogeneously charged brush has a slightly less sharp ionization and that the increase occurs over a slightly larger pH range. However, the curves appear in very similar positions compared with those of the default homogeneous system, and the results do not come significantly closer to the experimental data.

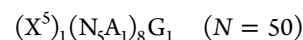
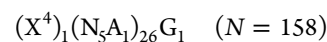
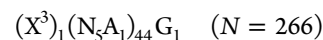
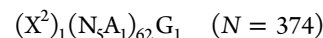
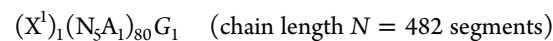
In the default system, we assumed that all polymer chains were equally long. Of course in practice there always is a significant polydispersity of the chains. Therefore, it is timely to implement a model wherein the chains are polydisperse. Here we consider a Schulz–Zimm distribution of polymer chain lengths.<sup>24–26</sup>

$$P(x, N_i) = \frac{x^{x+1}}{\Gamma(x+1)} \frac{N_i^{x-1}}{N_n^x} \exp\left(-\frac{xN_i}{N_n}\right) \quad (29)$$

in which  $P(N_i)$  is the probability of chains with degree of polymerization  $N_i$ ,  $N_n$  is the number-average degree of polymerization and  $x$  defines the broadness of the distribution.  $\Gamma(x+1)$  is the gamma function, which is equal to  $x!$  for integer values of  $x$ . The polydispersity is directly related to  $x$  by

$$\frac{M_w}{M_n} = \frac{x+1}{x} \quad (30)$$

Since a distribution of polymer chains with all the possible number of segments per chain is impracticable to compute, we have considered distributions with just a few different chain lengths, with increments of 100 segments. Hence we approximate the Schulz–Zimm distribution by taking five different chains such that the largest chain had the same composition of the monodisperse homogeneously distributed charge case. More specifically the sequences were:



The grafting density for each member in this distribution was calculated with the probability given by Schulz–Zimm functions for each of these chain lengths (eq 29). The corresponding  $\theta$  values were found by multiplying the grafting density by the chain length. Finally the distribution was normalized so that the



sum of the  $\theta$  parameters of the individual polymers is  $3 \times 10^5$ , as mentioned in the Molecule Parameters.

We have used the Schulz–Zimm function with a  $N_n$  parameter of 150, and a polydispersity parameter  $\alpha = 1$ , which leads to a polydispersity index  $M_w/M_n = 2$ , if all the polymer chains with lengths from 1 to  $\infty$  were used. The actual polydispersity index of the set of five chains that we used was  $M_w/M_n = 1.70$ . Again the overall charge density in the polydisperse case was set equal to that of the default case.

In Figure 6, we have also included the results of the polydisperse brush (dotted curves). Typically it is seen that the dotted curve give a slightly larger shift of the apparent  $pK_w$  that is, they are slightly closer to the experimental titration curve than the inhomogeneously charged brush (dashed lines). This can be explained because in the polydisperse brush there are many short chains and fewer long ones. Hence the polydisperse brush puts effectively more polymer segments near the core. The larger chain density near the core implies a larger density of chargeable segments near the core. Hence we should expect a more pronounced shift of the titration curve, placing the model predictions a bit closer to the experimental results.

The ionic strength dependence of the titration curves for the various models can be seen from the comparison of Figures 6a–c. For low ionic strength (part a), the models can be distinguished. However, for high ionic strength (part c), the differences vanish. We can understand this because at high ionic strength the charges are screened and the degree of dissociation is not a strong function of how the charge is distributed along the chain (inhomogeneously charged brush) or in the polydisperse brush. Yet at all three ionic strength conditions the modeling results deviate from the experimental data.

We collected the ionic strength dependence of the height of the brush for all three models (Figure 7), that is for the default homogeneously charged brush (solid curve) the inhomogeneously charged brush (dashed curve), and the polydisperse brush (dotted curves) and compared the results to the experimental data (points). In this figure, panel a is for  $T = 288$  K, panel b for  $T = 306$  K, and panel c for  $T = 318$  K ( $\chi_{WN} = 0.2, 0.8$ , and  $1.2$ , respectively). We selected pH values of 7.5, 5, and 4. As compared to Figure 5, we show results for a wider ionic strength range.

For all three models, we observe qualitatively the same behavior. As already shown in Figure 5, typically the shell height decreases with increased ionic strength. This dependence is qualitatively in agreement with the experimental data. The screening of the charges by the salt leads to a reduction of the repulsion between the charges. However, at pH = 5.0 and  $\chi_{WN} = 0.8$  (Figure 7b), we can also see a brush collapsed in the absence of salt that expands upon the initial increase of ionic strength. This behavior indicates that the system is in an osmotic regime. Upon continuing to increase the ionic strength, we change to the salted brush regime and the usual decrease in height due to charge screening is observed.

We can see some noticeable differences for the height as a function of the ionic strength between the default homogeneous brush (solid curve) and inhomogeneously charged brush (dashed curve), particularly in the osmotic regime region previously mentioned at pH = 5.0 and  $\chi_{WN} = 0.8$ . We can also see some differences between monodisperse and polydisperse homogeneous systems. However, these differences are relatively small and the same trends can be observed in all cases. The experimental data points qualitatively follow the modeling

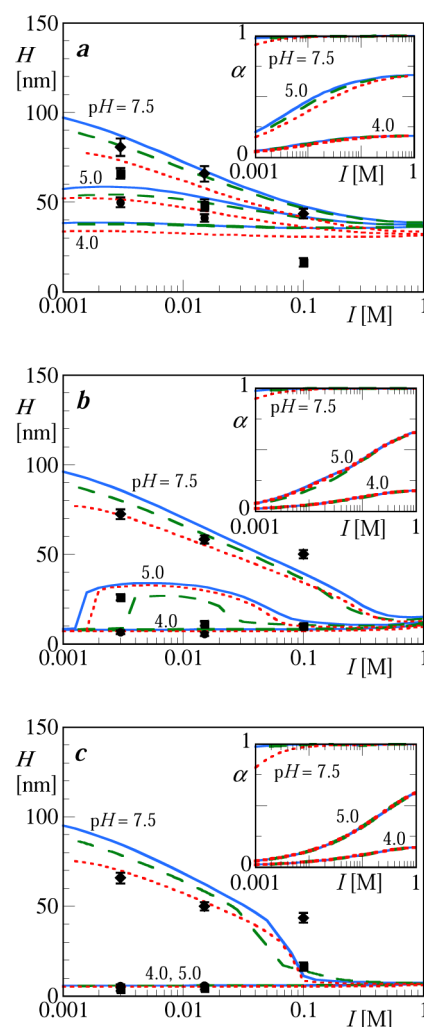


**Figure 7.** Modeled curves showing the cases of both homogeneously distributed segments along the chains (blue solid curves), inhomogeneously charged brush (green dashed curves), and polydisperse brush (red dotted curves) compared with the experimental DLS data (data points) at temperature  $T = 288.15$ ,  $306.15$ , and  $318.15$  K. Brush height  $H$  as a function of ionic strength  $I$ . (a)  $\chi_{WN} = 0.2$ ,  $T = 288.15$  K; (b)  $\chi_{WN} = 0.8$ ,  $T = 306.15$  K; (c)  $\chi_{WN} = 1.2$ ,  $T = 318.15$  K; DLS data at pH = 4.0 (●), pH = 5.0 (■), and pH = 7.5 (◆). Inset: degree of ionization  $\alpha$  as a function of ionic strength.

results. Unfortunately the data is not precise enough to discriminate between the models.

The insets in Figure 7 show the average degree of dissociation of the acid groups as a function of the ionic strength for the pH values indicated. As can be seen from these insets, an increase of the ionic strength generally leads to an increase of the average degree of dissociation. These dependences are in line with the results discussed earlier. The purpose of these insets is to prove that the models do not differ much in this respect. Especially at high ionic strength the differences are extremely small. Only at low ionic strength and medium to high pH values, the positioning of the charges along the chains and the degree of polydispersity matter somewhat. The ionization thus seems to occur in a slightly wider pH range in both the heterogeneous and the polydisperse cases, indicating a slightly larger polyelectrolytic effect, although not as large as the one observed with the experimental data (here comparison with experimental data is not shown).

Finally, we have plotted the height of the brush for the three models as a function of the pH for three ionic strengths, namely (Figure 8a) 3, (Figure 8b) 15 and (Figure 8c) 100 mM. Results

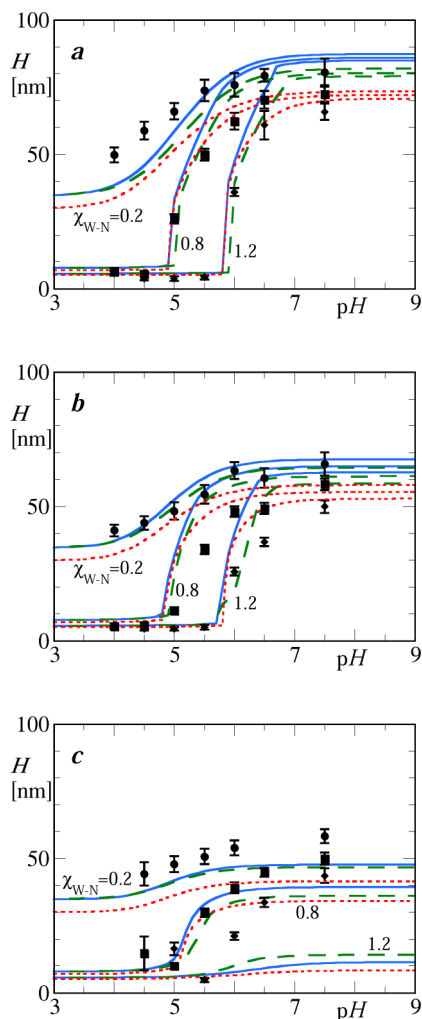


**Figure 8.** Brush height  $H$  as a function of pH. Blue solid curves: default system (homogeneous segments distribution along the chain); Green dashed curves: inhomogeneously charged brush; Red dotted lines: polydisperse system. (a) Ionic strength  $I = 3$  mM, (b)  $I = 15$  mM, and (c)  $I = 100$  mM. Modeled curves compared with the experimental DLS data at temperature  $T = 288.15$  (●),  $306.15$  (■), and  $318.15$  K (◆).

for low, intermediate, and higher  $\chi_{WN}$  parameters, corresponding to an increasing temperature, are presented as indicated. Also in this comparison the three models are only marginally different. Close inspection shows that all three models deviate in a similar way from the experimental data (points in Figure 8). Typically the transition from the collapsed brush to the expanded brush (with increasing pH) is more abrupt in the model than found experimentally. The difference between experimental data and the models is relatively large for the high ionic strength cases (Figure 8c) possibly indicating that nonelectrostatic interactions are not sufficiently accurately taken into account in the models.

## DISCUSSION

In the hydrophobic polyelectrolyte brush there are competing forces. Charges in the brush have the tendency to hydrate the brush. Poor solvent conditions, on the other hand, dehydrate the brush. We see that with increasing pH, decreasing ionic strength

and decreasing the temperature leads to the swollen state of the brush. A low pH, high ionic strengths, and high temperature lead to the collapse of the brush. Hence the hydrophobic polyelectrolyte brush responds to these three parameters. The SCF theory qualitatively and arguably semiquantitatively describes these effects, albeit an exact match with experimental data is not possible. It is instructive to briefly mention some complications.

There are significant difficulties in assessing the height of a brush, especially when microphase-segregated structures are present. Above we have shown that the first or second moment of the end-point distribution is usually not an accurate prediction of the height of the brush. Instead we estimated the height of the brush by recording at which height the brush reached a low volume fraction threshold value. When we use this measure for the height, we found an artificial jump-like behavior of the height whereas in reality the height variation is smooth. Nevertheless, we believe that it reasonably accounts for the hydrodynamic effect of a dilute corona layer. We can imagine that less *ad hoc* procedures may lead to a better prediction.

We see significant deviations in height compared to the experimental data, especially at high ionic strengths and higher temperatures (see, for example, Figures 5c or 8c). This might be happening because SF-SCF theory only takes into account average radial concentrations, failing to describe the possibility of localized phenomena. For instance, it was observed in molecular dynamics simulations of polyelectrolyte stars that the corona chains may bundle laterally at high ionic strengths instead of collapsing over the core.<sup>18</sup> Such a bundling might explain why a significant hydrodynamic radius is experimentally observed, while the model predicts a much lower brush height.

Also, in such a bundling, we may have the formation of hydrophobic local domains, which may be more difficult to ionize due to the lack of hydration. Thus, there is a solvation effect involved in the ionization of the acid groups. We have speculated above that the brush at room temperature is already in the “transition” state, where the brush is in a microphase segregated state. This could explain why the experimental titration curves have such a large shift of the apparent  $pK_a$ . In this case, we should reconsider the relation between the temperature and the FH parameter.

Next there is the possibility that the acid groups are much less ideally distributed than we considered in the theoretical models. More specifically, it is possible that the acid groups are polymerized together in blocks (which is very likely since the reactivity of MA is higher than that of NIPAM, and it has been shown that both MA and NIPAM prefer to polymerize with another MA or NIPAM monomer, respectively<sup>27–29</sup>). Such local high charge densities can explain in part the experimental data. For example, it can explain the relatively large polyelectrolyte effect (shift of the apparent  $pK_a$ ). In a mean field model, such local (along the chain) correlation between charges and their probability to be ionized can not be properly accounted for.

The structure of particles covered by a hydrophobic polyelectrolyte brush in reality is more complex and rich than predicted by SCF models, and clearly we cannot rely in SF-SCF modeling alone to predict their behavior.

## CONCLUSION

We have synthesized core–shell polymer particles with a glassy PMMA core decorated with an ionizable stimuli responsive polymer brush-like shell composed of PNIPAM and methacrylic acid comonomers, with low size dispersity. We have studied their

structural characteristics in water by DLS and potentiometric measurements, and modeled the behavior of the brush using the SF-SCF approach.

The particles show a volume phase transition (observed by DLS), which is pH and ionic strength dependent. We also observed (by potentiometry) a strong polyelectrolyte effect, that is, a shift of the apparent  $pK_a$  extracted from the degree of dissociation of the acid groups as a function of the pH, already at room temperature (an effect also seen in the DLS data).

Using SF-SCF, we modeled the particle shell as a brush of polymer chains with homogeneously distributed acid segments intercalated with a constant number of neutral thermoresponsive segments, and also as an heterogeneous brush, with a greater proportion of acid segments near the core, and the case of polydisperse systems.

The modeling results show us a rich internal structure of the hydrophobic polyelectrolyte brush, especially near the collapse transition, where we find a microphase segregated structure. The theoretical predictions follow the experimental data qualitatively. There is, however, some quantitative disparity between theory and experiments that diminishes only slightly when we modeled the system as heterogeneous or polydisperse. We can attribute this difference, in part, to the unknown polydispersity of the chains, the unknown distribution of the charges, or to experimental complications. However, these deviations tell us that it is also very likely that there are significant problems in the mean field theory. We believe these problems are related to the fact that the mean field theory focuses solely on the radial distributions and ignores the possibility of formation of local lateral inhomogeneities in the partially collapsed brushes. The differences between the experimental data and the model results show that, even at room temperature, the brush is already behaving nonideally.

## AUTHOR INFORMATION

### Corresponding Author

\*(S.P.C.A.) E-mail: sergio.c.alves@tecnico.ulisboa.pt.

### Notes

The authors declare no competing financial interest.

## ACKNOWLEDGMENTS

We wish to thank Remco Fokkink (Wageningen University) for his technical support in the DLS measurements, and Leila Moura (Instituto Superior Técnico) for her help in the synthesis of the P(N-MA) nanoparticles. This work was partially supported by Fundação para a Ciência e a Tecnologia (FCT, Portugal) and POCI 2010 (FEDER) through project PTDC/CTM-NAN/115110/2009. S.P.C.A. acknowledges funding by a postdoctoral grant SFRH/BPD/74654/2010 (FCT, Portugal). J.P.P. acknowledges funding by IBB/CBME (LA, FEDER/POCI 2010/PEst-OE/EQB/LA0023/2011) and a Sabbatical Grant SFRH/BSAB/855/2008 (FCT, Portugal).

## REFERENCES

- (1) Stuart, M. A. C.; Huck, W. T. S.; Genzer, J.; Müller, M.; Ober, C.; Stamm, M.; Sukhorukov, G. B.; Szleifer, I.; Tsukruk, V. V.; Urban, M.; et al. Emerging Applications of Stimuli-responsive Polymer Materials. *Nat. Mater.* **2010**, *9*, 101–113.
- (2) Motornov, M.; Roiter, Y.; Tokarev, I.; Minko, S. Stimuli-Responsive Nanoparticles, Nanogels and Capsules for Integrated Multifunctional Intelligent Systems. *Prog. Polym. Sci.* **2010**, *35*, 174–211.
- (3) Parasuraman, D.; Serpe, M. J. Poly (N-Isopropylacrylamide) Microgels for Organic Dye Removal from Water. *ACS Appl. Mater. Interfaces* **2011**, *3*, 2732–2737.
- (4) Moura, L.; Martinho, J. M. G.; Farinha, J. P. S. DNA Hybridization in Thermoresponsive Polymer Nanoparticles. *ChemPhysChem* **2010**, *11*, 1749–1756.
- (5) Martinho, J. M. G.; Prazeres, T.; Moura, L.; Farinha, J. P. S. Fluorescence of Oligonucleotides Adsorbed onto the Thermoresponsive Poly(Isopropyl Acrylamide) Shell of Polymer Nanoparticles: Application to Bioassays. *Pure Appl. Chem.* **2012**, *28*, 5802–5809.
- (6) Prazeres, T.; Farinha, J. P. S.; Martinho, J. M. G. Control of Oligonucleotide Distribution on the Shell of Thermo-Responsive Polymer Nanoparticles. *J. Phys. Chem. C* **2008**, *112*, 16331–16339.
- (7) Pinheiro, J. P.; Moura, L.; Fokkink, R.; Farinha, J. P. S. Preparation and Characterization of Low Dispersity Anionic Multiresponsive Core–Shell Polymer Nanoparticles. *Langmuir* **2012**, *28*, 5802–5809.
- (8) Fleer, G. J.; Stuart, M. A. C.; Scheutjens, J. M. H. M.; Cosgrove, T.; Vincent, B. *Polymers at Interfaces*, 1st ed.; Chapman & Hall: London, Great Britain, 1993.
- (9) Currie, E.; Wagemaker, M.; Cohen Stuart, M.; van Well, A. Structure of Grafted Polymers, Investigated with Neutron Reflectometry. *Physica B* **2000**, *283*, 17–21.
- (10) Borisov, O. V.; Zhulina, E. B.; Leermakers, F. A. M.; Ballauff, M.; Müller, A. H. E. Conformations and Solution Properties of Star-Branched Polyelectrolytes. *Adv. Polym. Sci.* **2011**, *241*, 1–56.
- (11) Borisov, O.; Zhulina, E.; Leermakers, F.; Müller, A. Self-Assembled Structures of Amphiphilic Ionic Block Copolymers: Theory, Self-Consistent Field Modeling and Experiment. *Adv. Polym. Sci.* **2011**, *241*, 57–129.
- (12) Leermakers, F.; Rabinovich, A.; Balabaev, N. Self-Consistent Field Modeling of Hydrated Unsaturated Lipid Bilayers in the Liquid-Crystal Phase and Comparison to Molecular Dynamics Simulations. *Phys. Rev. E* **2003**, *011910*/1–17.
- (13) Postmus, B.; Leermakers, F.; Cohen Stuart, M. Self-Consistent Field Modeling of Adsorption From Polymer/Surfactant Mixtures. *Langmuir* **2008**, *24*, 6712–6720.
- (14) Rud, O. V.; Mercurieva, A. A.; Leermakers, F. A. M.; Birshtein, T. M. Collapse of Polyelectrolyte Star. Theory and Modeling. *Macromolecules* **2012**, *45*, 2145–2160.
- (15) Iakovlev, P. A. *Core-Shell Particles Experiments and Self-Consistent Field Modelling*. Ph.D. thesis; Wageningen University: Wageningen, The Netherlands, 2011.
- (16) Jusufi, A.; Likos, C. Colloquium: Star-Branched Polyelectrolytes: The Physics of their Conformations and Interactions. *Rev. Mod. Phys.* **2009**, *81*, 1753–1772.
- (17) Ballauff, M. Spherical Polyelectrolyte Brushes. *Prog. Polym. Sci.* **2007**, *32*, 1135–1151.
- (18) Košovan, P.; Kuldová, J.; Limpouchová, Z.; Procházka, K.; Zhulina, E. B.; Borisov, O. V. Molecular Dynamics Simulations of a Polyelectrolyte Star in Poor Solvent. *Soft Matter* **2010**, *6*, 1872–1874.
- (19) Edwards, S. F. The Statistical Mechanics of Polymers with Excluded Volume. *Proc. Phys. Soc.* **1965**, *85*, 613–624.
- (20) Prazeres, T. J. V.; Beija, M.; Fernandes, F. V.; Marcelino, P. A. G.; Farinha, J. P. S.; Martinho, J. M. G. Determination of the Critical Micelle Concentration of Surfactants and Amphiphilic Block Copolymers Using Coumarin 153. *Inorg. Chim. Acta* **2012**, *381*, 181–187.
- (21) Ferguson, C. J.; Russell, G. T.; Gilbert, R. G. Synthesis of Latices with Polystyrene Cores and Poly(Vinyl Acetate) Shells. 1. Use of Polystyrene Seeds. *Polymer* **2002**, *43*, 4557–4570.
- (22) Zhulina, E. B.; Borisov, O. V. Structure and Interaction of Weakly Charged Polyelectrolyte Brushes: Self-Consistent Field Theory. *J. Chem. Phys.* **1997**, *107*, 5952–5967.
- (23) Zhulina, E. B.; Borisov, O. V.; Birshtein, T. M. Structure of Grafted Polyelectrolyte Layer. *J. Phys. II* **1992**, *2*, 63–74.
- (24) de Vos, W. M. *Brushes and Particles*. Ph.D. Thesis. Wageningen University: Wageningen, The Netherlands, 2009.
- (25) Schulz, G. V. Über die Kinetik der Kettenpolymerisationen. *Z. Phys. Chem.* **1939**, *B43*, 25–46.



(26) Zimm, B. H. Apparatus and Methods for Measurement and Interpretation of the Angular Variation of Light Scattering and Preliminary Results on Polystyrene Solutions. *J. Chem. Phys.* **1948**, *16*, 1099–1116.

(27) Hoare, T.; Pelton, R. Highly pH and Temperature-Responsive Microgels Functionalized with Vinylacetic Acid. *Macromolecules* **2004**, *37*, 2544–2550.

(28) Xue, W.; Champ, S.; Huglin, M. B. Observations on some Copolymerizations Involving N-Isopropylacrylamide. *Polymer* **2000**, *41*, 7575–7581.

(29) Shibayama, M.; Tanaka, T. J.; Han, C. C. Small Angle Neutron Scattering Study on Weakly Charged Temperature Sensitive Polymer Gels. *J. Chem. Phys.* **1992**, *97*, 6842–6854.